Insights on CaTiS3 films grown by pulsed laser deposition

Thomas Fix, Slimane Raissi, Dominique Muller, Corinne Bouillet, Daniele Preziosi, Abdelilah Slaoui

Insights on $CaTiS_3$ films grown by pulsed laser deposition

T. Fix[1], S. Raissi[1], D. Muller[1], C. Bouillet[2], D. Preziosi[2], A. Slaoui[1]

[1] ICube laboratory, CNRS and Université de Strasbourg, 23 rue du Loess, 67037 Strasbourg, France

[2] Institut de Physique et Chimie des Matériaux de Strasbourg (IPCMS), UMR 7504 CNRS and Université de Strasbourg, 23 rue du Loess, BP 43, F-67034 Strasbourg Cedex 2, France

* Corresponding author. Tel.: +33 388106334, Fax +33 388106548. E-mail address: tfix@unistra.fr

Abstract

We attempt to grow perovskite $CaTiS_3$ by pulsed laser deposition (PLD) on various substrates using a $CaS:TiS_2$ target. Using Al_2O_3 (0001) substrates at 600°C deposition temperature in vacuum, $Ca_{1.0}Ti_{1.05}S_{2.48}O_y$ stoichiometry is measured by Energy-dispersive X-ray spectroscopy (EDS) and $Ca_{1.0}Ti_{1.0}S_{2.0}O_{0.7}$ by Rutherford Backscattering Spectrometry (RBS). This indicates that when the films are grown in vacuum at moderate temperature, a high amount of S can be transferred from the target to the film. While no phase segregation of CaS and TiS_2 could be observed, no perovskite $CaTiS_3$ phase could be obtained, but rather a phase governed by van der Waals interactions. The films show a highly doped n-type semiconductor behavior with absorption coefficient in the 10^5 cm^{-1} range at 350-2500 nm but no surface photovoltage signal. This work should stimulate further experimental efforts in PLD growth of chalcogenides and chalcogenide perovskites.

Keywords: thin films; sulphide materials

1. Introduction

In the world of inorganic materials, while so many materials have already been discovered and reported, the class of chalcogenide perovskites and related ABS_3 sulfides forms an exceptional reservoir of emerging materials. In ABX_3 structures, more covalent B-X bonds correspond to a lower difference in electronegativity between B and X which allows better charge transport in the material and lower bandgap [1]. As an example, the experimental bandgap of $BaZrO_3$ is 2.87 eV while it falls to 1.75 eV for $BaZrS_3$ [1] because S has lower electronegativity than O. While halide perovskites are outstanding materials for photovoltaic and optoelectronic applications, partly due to the low electronegativity difference between Pb and I in $MAPbI_3$ (MA=methylammonium), oxide perovskites seem far behind despite their exceptional multifunctional properties among to name a few superconductivity, multiferroicity and high spin polarization, combined with high stability [2]. Sulfur and selenium are important elements for thin film photovoltaics because of their presence in the $CuIn_xGa_{1-x}(S,Se)_2$ (CIGS) absorber. When included in chalcogenide perovskites, they can form compounds rather stable in air and water as reported for $BaZrS_3$ [3, 4], as opposed to $MAPbI_3$. As well, oxidation in air starts only in the 500-600 °C range [5]. Unfortunately, not all ABO_3 starting material can be envisaged as ABS_3 perovskites due to phase formation issues. Still, 26 different perovskite chalcogenides are reported in the review of Sopiha *et al.* [4].

Distorted perovskite $CaTiS_3$ (CTS) has been reported in 2015 as a promising candidate for photovoltaics with a bandgap of about 0.9 eV [6]. Since then there has been no experimental report on CTS material while a direct bandgap of 0.90 eV was confirmed using first-principles calculations in an orthorhombic structure [7]. The stability of putative chalcogenide perovskites is well discussed in [4]. In the case of CTS, while the Goldschmidt tolerance factor t is about 0.92, which is in the range of $0.7 < t < 1.1$ where stable perovskites can form, the octahedral factor μ is about 0.33, which is lower than the minimum value of 0.41 for stable perovskite structure. As well, the computed value of formation energy of $GdFeO_3$-type $CaTiS_3$ perovskite with respect to binaries (H_f) is reported to be unfavorable for perovskite

formation while the $CaTiS_3$ perovskite ground state is low enough, only 40 meV $f.u.^{-1}$ higher than the needle-like phase which is calculated to be the most stable phase [4, 6, 8].

While $CaTiS_3$ has not been reported experimentally, a related compound has been more extensively studied, $SnTiS_3$. It has been reported in the form of a crystal as a self-assembled van der Waals heterostructure of SnS and TiS_2, referred to as a misfit layer compound because the alternating layers form a heterostructure with a less symmetric crystal structure [9-11].

Because pulsed laser deposition (PLD) is well known to enable the formation of metastable phases, as in the case for example of h-$TbMnO_3$ less stable than o-$TbMnO_3$ [12], we attempt in this work to obtain $CaTiS_3$ perovskites. We use PLD for film growth, using a target mixing the two CaS and TiS_2 precursors. Calcium sulfide CaS is an insulator with a bandgap from 2.5 to 4.5 eV, which provides high luminescence when doped with rare earth elements [13]. TiS_2 finds applications in batteries and is either described as a metal or semimetal, or a degenerate semiconductor, although a positive temperature dependence of resistivity is often observed [14-16]. In the following text, we will call the thin films deposited using the CaS : TiS_2 target by the acronym CTS.

2. Experimental procedure

PLD fabrication

The target for PLD deposition was made by mixing the required quantities of CaS (purity 99.9%, Alfa Aesar) and TiS_2 (purity 99.9%, Sigma Aldrich) and fabricating a 1'' pellet which was pressed isostatically with an actual pressure on the target of 460 MPa (Cold Isostatic Pressing Press from MIT Corporation YLJ-CIP-500M-30). The target was then mounted in the PLD chamber without any further treatment. The isostatic press is a key feature for obtaining a sulfur rich PLD target without the need of annealing under sulfur-rich atmosphere which would require special equipment and safety measures.

The substrates used for PLD deposition were $SrTiO_3$ (001) (STO), Al_2O_3 (0001) (ALO), $MgAl_2O_4$ (001) (MAO), TiO_2 (001) and (100) from Crystal GmbH, and fused quartz. The PLD process was performed

using a KrF laser (248 nm) with a 10 Hz repetition rate and a laser fluence of around 1-2 J/cm^2 (typically 18000 pulses). The depositions were carried out at 600-900°C in vacuum (typically $5 \cdot 10^{-6}$ – $1 \cdot 10^{-5}$ mbar during deposition while at high temperature). The target-substrate distance was fixed at 55 mm. Around 15 samples were deposited by PLD for the study.

Film characterization

Films grown by PLD on crystal substrates were investigated using at room temperature a Rigaku SmartLab diffractometer equipped with a monochromatic source delivering a Cu $K_{\alpha 1}$ incident beam (45 kV, 200 mA, 0.154056 nm). The same apparatus was used for x-ray diffraction (XRD) and x-ray reflectivity (XRR). Rutherford Backscattering Spectrometry (RBS) was used to determine atomic composition and thickness of the layers by using 1.5 MeV He^+ particles provided by the Van de Graaff accelerator (HVEE KN4000) facility of ICube. The analysis of the spectra was performed using the SIMNRA tool. The optical properties were obtained by measuring transmittance with a UV–vis-IR Perkin-Elmer Lambda 19 spectrophotometer. The optical properties and thickness of the films were also investigated by spectroscopic ellipsometry using a HORIBA Uvisel Lt M200 FGMS (210–880 nm) apparatus. The dispersion formula for CTS films is based on the double Tauc-Lorentz model [17]. The goodness-of-fit value (Chi Square χ^2) was 3.2 for a CTS film thickness of around 80 nm. Photoluminescence (PL) was carried out at room temperature using an excitation at 355 nm with a frequency-tripled neodymium-doped yttrium aluminum garnet (Nd-YAG) laser. The laser pulse duration, frequency and power were 10 ns, 20 kHz and up to 45 mW (7 W cm^{-2}), respectively. The PL signal was collected by means of a concave mirror into an optical fiber and analyzed by a multichannel CCD. The PL signal was integrated over time for a duration of 600 ms.

The surface of the films was investigated using atomic force microscopy (AFM) with a NT-MDT Smena B AFM in tapping mode. Scanning electron microscopy (SEM) was performed with a JEOL JSM-IT200LA apparatus and the stoichiometry was checked by Energy-dispersive X-ray spectroscopy (EDS). Hall

effect was measured using an ECOPIA HMS-5000 system at room temperature. Resistance vs. temperature was measured with a Physical Properties Measurement System (Dynacool, Quantum Design) from 300 K to 5 K using a van der Pauw configuration. Kelvin Probe (KP) and Surface PhotoVoltage (SPV) measurements were performed with a single point Kelvin Probe system (KP Technology KP020) with a 2 mm diameter gold tip, and using a halogen source with calibrated illumination for white light SPV.

To further investigate the structural properties of the films, Transmission Electron Microscopy (TEM) was performed using a JEOL 2100 F microscope, operating at 200 kV, with a point to point resolution of 0.2 nm and a corrector on the condenser lenses, to perform high-resolution imaging. The sample was prepared, as a cross section in the STO substrate [100] zone axis, using the focused ion beam (FIB) technique.

3. Results and discussion

Films were grown first on STO (001) in vacuum at different deposition temperatures from 600°C to 900°C using a target containing the CaS and TiS_2 precursors as described in the experimental procedure. Peaks of CaS and TiS_2 are identified as shown in Figure 1. This is confirmed by TEM observations described later in the text. As shown in Table 1, the films grown on STO (001) in vacuum at 600°C and 700°C contain an appropriate amount of S as determined by EDS. This means that the preservation of stoichiometry due to the so-called congruence of PLD is also valid for the S element under certain conditions. The films grown at 800°C and 900°C show a progressive decrease of S molar amount, which is caused by the re-evaporation of sulfur due to high vapor pressure. The Ti stoichiometry cannot be determined for these samples because of the presence of Ti in the STO substrate; the O stoichiometry cannot also be determined by EDS. However, the film grown on ALO (0001) indicates that the Ca and Ti elements are present in the right composition according to EDS: $Ca_{1.0}Ti_{1.05}S_{2.48}O_y$. This is confirmed by RBS that indicates a stoichiometry of $Ca_{1.0}Ti_{1.0}S_{2.0}O_{0.7}$, revealing the amount of oxygen in the film on ALO (0001) (Figure S1 of Supplementary Information (SI)). Coming

back to the 800°C and 900°C samples on STO, the decrease of S amount in the films is accompanied in the XRD shown in Figure 1 by the appearance of $CaTiO_3$ (00l) peaks. The $CaTiO_3$ (002) peak corresponds to a pseudocubic out-of-plane parameter of 0.381 $\pm$0.001 nm, very close to the pseudocubic out-of-plane parameter of perovskite $CaTiO_3$ (0.3820 nm, ICDD 04-007-5451). This indicates that there is no incorporation of S in the $CaTiO_3$ phase that is formed. $CaTiO_3$ can form because at high temperature the base vacuum pressure is higher and oxygen is more reactive to form the $CaTiO_3$ phase. The CaS (002) and (004) peak positions are not moving when increasing the deposition temperature. This can indicate again no incorporation of S in the corresponding $CaTiO_3$ lattice. However, when looking at TiS_2 (001) there is a small progressive shift towards higher angles when going from 600°C to 800°C while the peak disappears at 900°C.

When now keeping the PLD growth at 600°C on STO (001) we introduce voluntarily an oxygen atmosphere at 10^{-3} or 10^{-2} mbar O_2. Figure 2 shows that when oxygen is introduced the CTS phase disappears and the $CaTiO_3$ (001) and (002) peaks appear. This shows that even a low oxygen atmosphere is detrimental to the formation of CTS. This is confirmed by Table 1 showing the absence of S in the samples grown in O_2.

In order to further understand the growth of the CTS phase, samples were grown on different crystal substrates such as MAO (001) and ALO (0001). Surprisingly, the same peaks of TiS_2 (001) and CaS (002) present with the STO (001) substrate can be observed with MAO and ALO substrates, and at the same angular position (Figure 3). This is unusual for the following reasons. STO is cubic and has a lattice parameter of 0.3905 nm while MAO is also cubic but with a lattice parameter of 0.8083 nm, i.e. two times 0.4015 nm. If there was epitaxy or texture of the CTS film, such a change in lattice parameters of the substrates would induce a change in the film out-of-plane parameter, unless fully relaxed. Concerning ALO, because this substrate has a R-3c space group it is not expected that CTS would grow in the same way as when grown of STO (001). As well, XRD of CTS on TiO_2 and fused quartz substrates provide the same texture of the films as with the other substrates. All these results indicate that the

CTS films grown do not obey to a traditional epitaxy as observed in many oxide systems using these crystal substrates. We will therefore use TEM to further investigate the films.

SEM observations indicated that the films grown on STO (001) are continuous, but with some splashing on the surface which is well known in the PLD process (Figure S2). Similar observations are made for films on ALO (0001) (Figure S3). When observing the sample in compositional mode, no phase segregation or elemental contrast can be observed apart from the previously mentioned splashing. This means that the surface of the films is homogeneous in composition at the scale achievable by the SEM. The surface quality is further investigated by AFM. Figure 4 shows an AFM topography image of a CTS sample on STO (001). The root mean square (RMS) roughness is 2.7 nm and the grain size is in the 100 nm range. This indicates that the films have a good surface quality for a film of around 80 nm thickness.

We now look into the optical properties of the films. The absorption coefficient of a CTS film is shown in Figure 5, and compared to a spectrum for diamond silicon. It is observed that CTS has a strong absorption coefficient in the 10^5 cm^{-1} range at 350-2500 nm. This is confirmed by spectroscopic ellipsometry and the refractive index and extinction coefficient could be determined (Figure S4 of SI). The Tauc plot in Figure 5 indicates a direct semiconductor with a bandgap of 1.59 eV. Photoluminescence measurements were also performed on CTS films grown on STO and ALO but no contribution other than the contribution of the substrates could be measured (Figure S5 of SI).

Now that good light absorption properties have been demonstrated, it is fundamental to focus in the electrical properties of the films. Because CTS is grown in vacuum, STO substrates are not appropriate for electrical measurements of the films because they become conductive due to oxygen deficiency. Therefore, the electrical measurements were performed on the ALO samples. Hall effect using CTS on ALO (0001) indicates a n-type conduction with a carrier density of - $3.4 \cdot 10^{22}$ cm^{-3}, mobility of 0.34 $cm^2V^{-1}s^{-1}$ and resistivity of $2.6 \cdot 10^{-3}$ $\Omega \cdot cm$. The value of carrier density is very high and the value of resistivity is very low which could suggest a metallic nature of the conduction of the film. To confirm this, we

performed resistance vs. temperature measurements of the film. Figure 6 shows a R-T measurement in the 300 K – 5 K range, showing that the sheet resistance increases when the temperature decreases, which is expected for a semiconductor.

As well, we measured the work function of the films using the Kelvin probe technique as detailed in the experimental section. The work function was measured to be in the 4.5-4.7 eV range. Using the same Kelvin probe apparatus while adding visible light on the sample during the measurement, surface photovoltage (SPV) can be measured. SPV is a widely used method to estimate the minority carrier diffusion length of semiconductors. It consists in measuring the potential of a semiconductor surface while generating electron-hole pairs with a light source. Typical highly efficient absorbers for solar cells provide a high SPV signal. Here, the photoactive response was negligible despite the high precision of the apparatus (Figure S6), indicating that the CTS films cannot be used as such as a photovoltaic absorber in a solar cell. This could be due to the high carrier density measured in the films.

Now that the basic properties of the films such as morphology, surface, optical, electrical properties are determined there is still some uncertainty about the structural arrangement of the CTS films. SEM has shown no phase segregation within the detection limits, tending to say that CaS and TiS_2 atomic planes are intricately combined within the structure. To do so, high resolution TEM is performed on a CTS sample on STO (001) as shown in Figure 7. It shows that the CTS film is crystalline but there are many Moiré fringes visible, of d-spacing of about 0.586 nm. Using the Moiré formula for TiS_2 d-spacing of 0.5705 nm and CaS d-spacing of 0.2811 nm yields a periodicity of 0.5541 nm quite close to the observed value. Moiré fringes are often observed in van der Waals superstructures that can be based on transition metal dichalcogenides [18]. The selected area electron diffraction (SAED) pattern is shown in Figure S7 of SI and the CTS film and substrate spots are identified, revealing the presence of d-spacing corresponding to CaS (002) and also TiS_2 (100) and (001), indicating that there is texture but multiple variants in plane for TiS_2 in the CTS film.

Conclusions

In conclusion, we attempted to grow perovskite $CaTiS_3$ films by PLD in the hope to benefit from the non-thermodynamic equilibrium nature of PLD growth and from the concept of epitaxial stabilization using various crystalline substrates. After having grown about 15 films we conclude that the putative perovskite phase of $CaTiS_3$ is not obtained experimentally. The PLD process is unexpectedly preserving relatively well the sulfur stoichiometry, if the deposition temperature is limited to 600-700°C and the films are deposited in vacuum. We found that the nature of the substrate has little influence on the diffraction patterns of the films, and therefore the growth of the films can be related to van der Waals interactions that are often encountered in chalcogenide materials. The films are of a highly-doped n-type semiconductor nature as observed by Hall effect and R-T measurements. TEM observations in cross section show that the films are crystalline but the observations in high resolution are disrupted by Moiré fringes. Surface photovoltage measurements indicate that the films are not photoactive, although the absorption coefficient is in the 10^5 cm^{-1} range and the direct bandgap is about 1.59 eV. This could be due to the high carrier density in the 10^{22} cm^{-3} range that can be a source of high Auger recombinations. The work should stimulate further experimental efforts into fabrication of emerging films of chalcogenide and chalcogenide perovskites by PLD.

Author contributions

TF conceptualization, methodology, investigation, writing – original draft, supervision; SR investigation, writing – review & editing; DM RBS measurements, writing – review & editing; CB TEM observations, writing – review & editing; DP investigation, writing – review & editing; AS writing – review & editing, project administration.

Declaration of Competing Interest

The authors declare that they have no known competing financial interests or personal relationships that could have appeared to influence the work reported in this paper.

Acknowledgments

222 The authors thank the XRD platform of IPCMS including M. Lenertz, and the staff of the C^3Fab platform
223 of ICube, including J. Bartringer for SEM and PL measurements and S. Roques. D. Troadec is greatly
224 thanked for FIB lamella preparation.

225 **Figure 1:** XRD θ-2θ patterns of films grown by PLD on STO (001) at different deposition temperatures,

226 and corresponding ICDD references for TiS_2 and CaS.

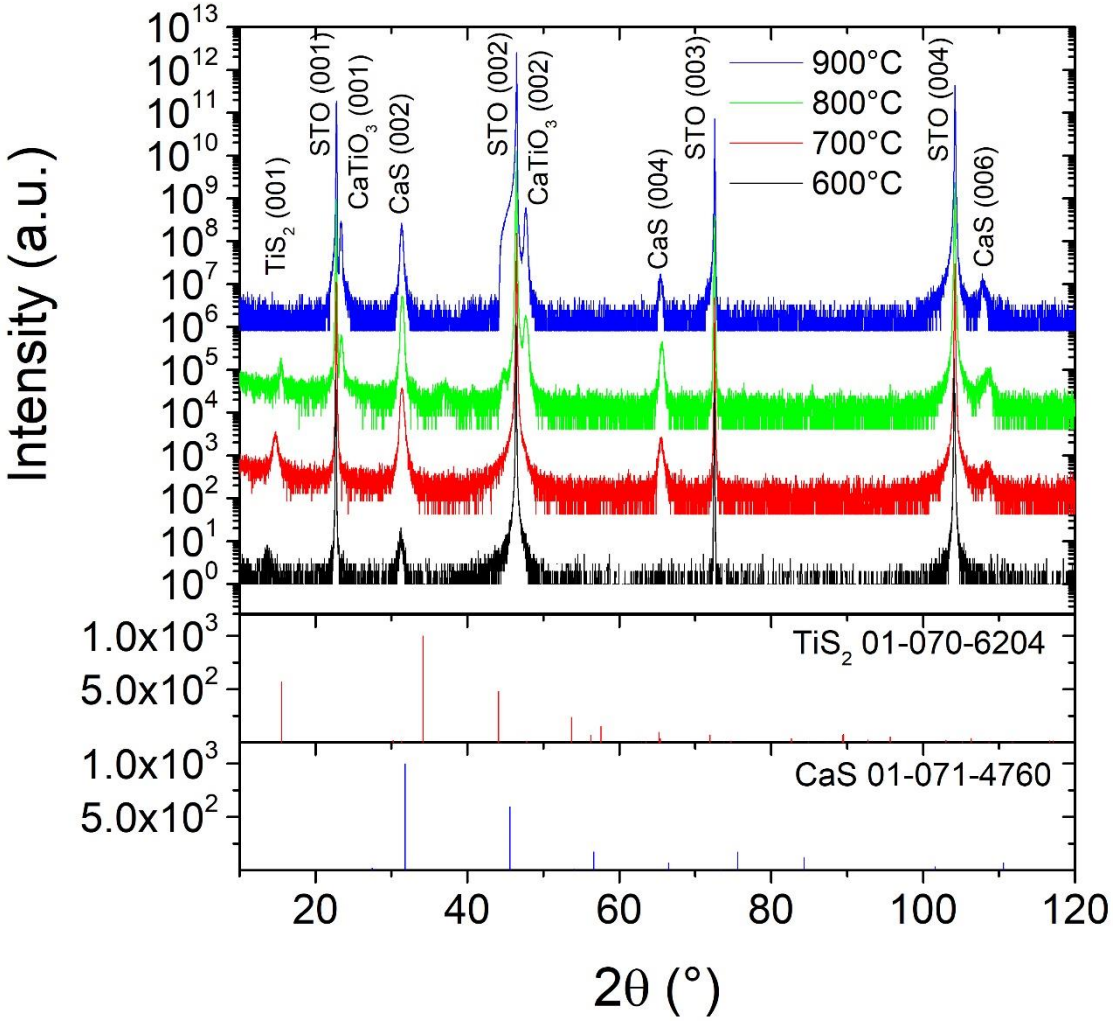

227

228

229 **Figure 2:** XRD θ-2θ patterns of films grown by PLD on STO (001) at 600°C in different atmospheres.

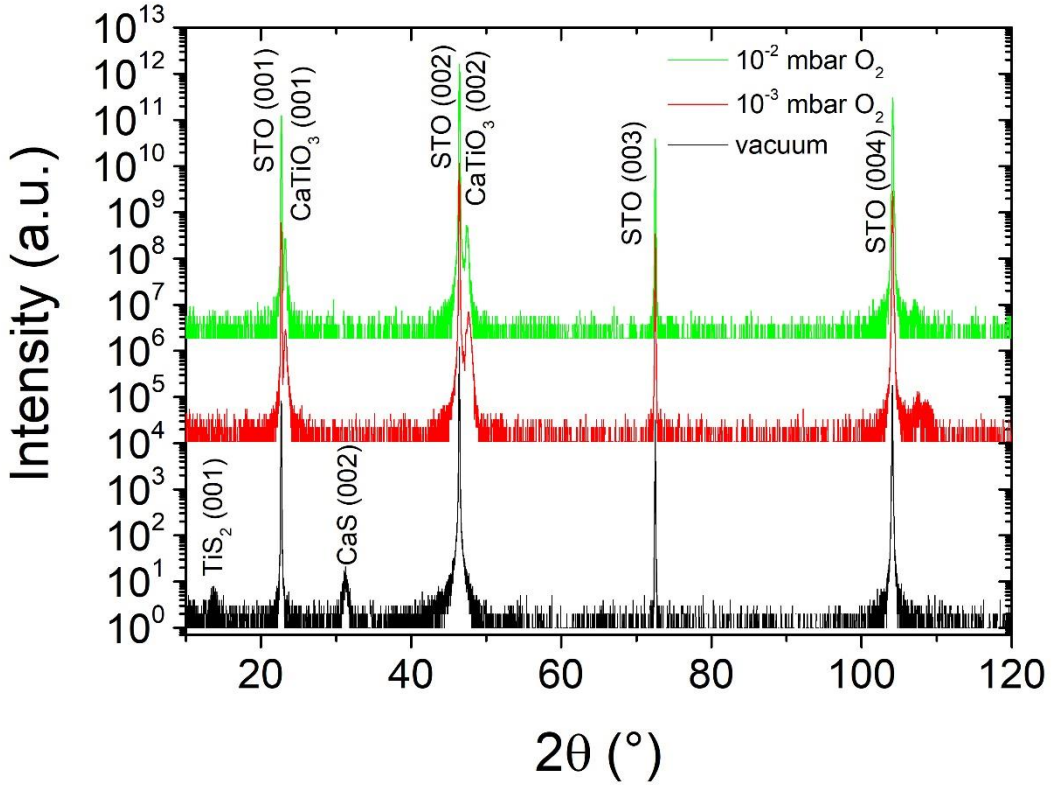

230

231 **Figure 3:** XRD θ-2θ patterns of films grown by PLD on different substrates at 600°C in vacuum.

232

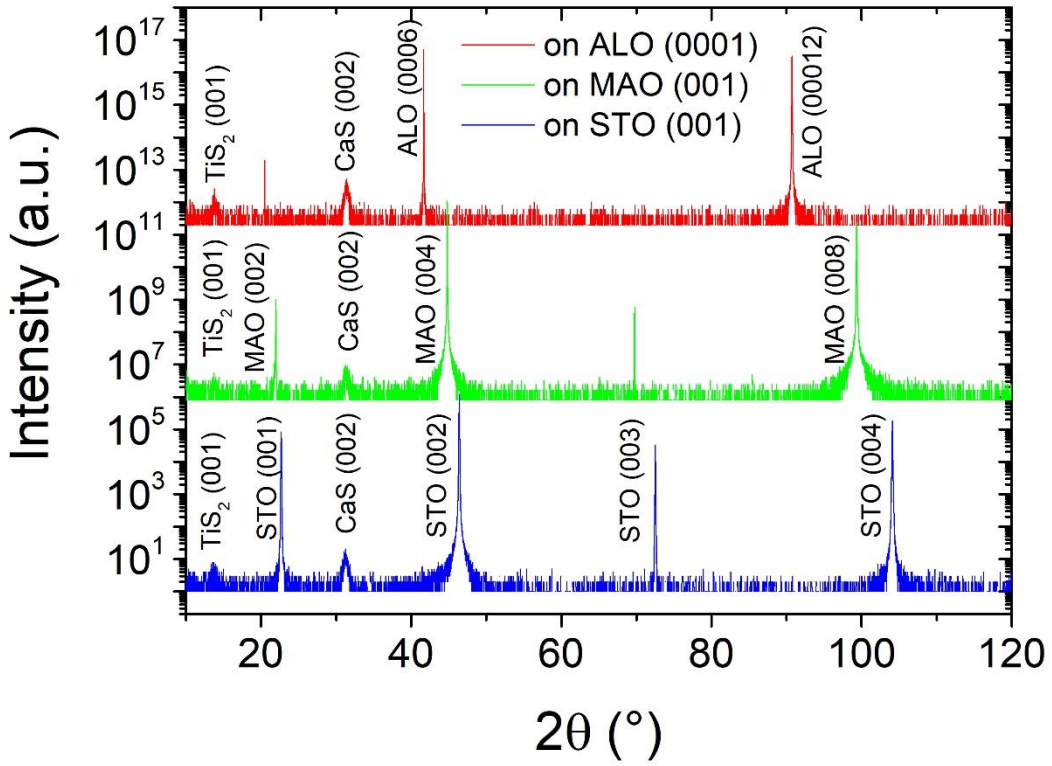

233

234

Figure 4: AFM topography image of a CTS sample grown on STO (001) at 700°C in vacuum.

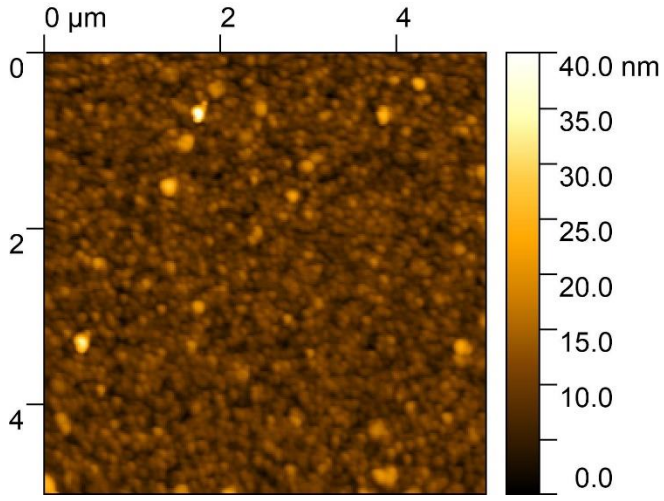

Figure 5: Absorption coefficient determined by UV-visible spectroscopy for a CTS sample grown on quartz at 600°C in vacuum. The reference for diamond silicon is taken from [19]. Inset: Tauc plot of CTS for a direct bandgap material.

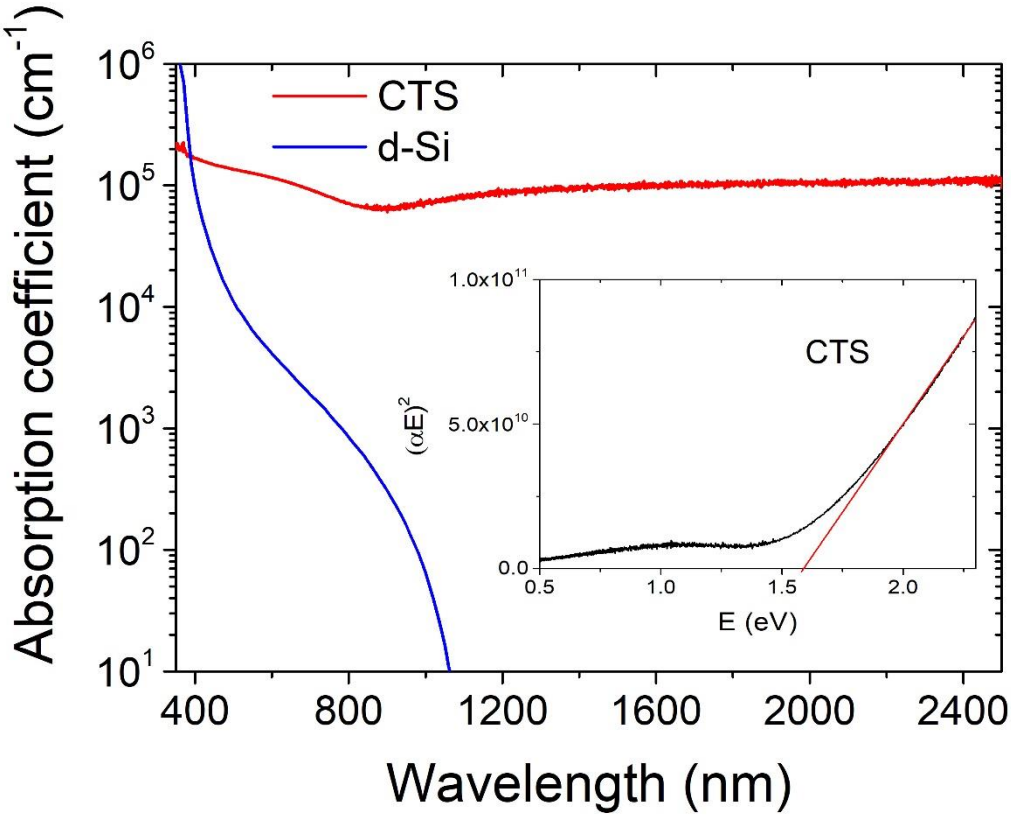

244 **Figure 6:** Sheet resistance vs. temperature of a CTS film grown on ALO (0001).

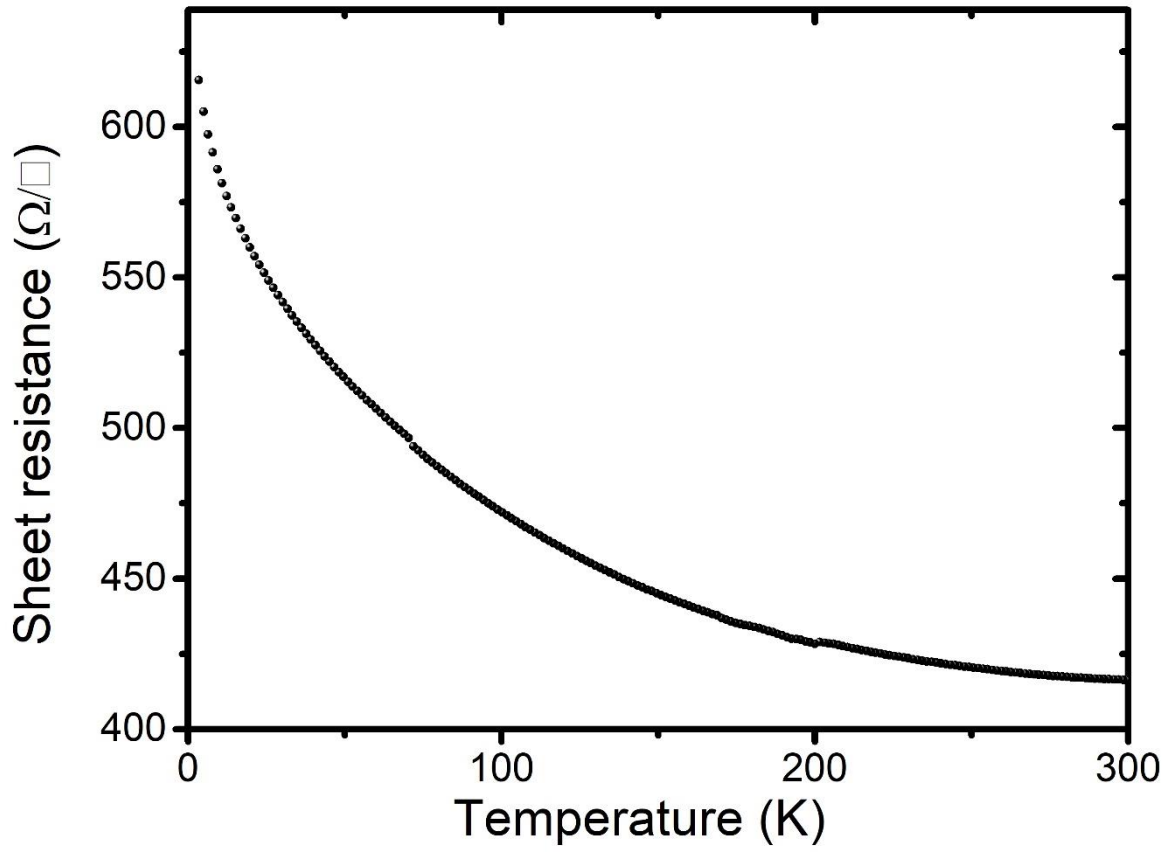

245

246

Figure 7: High resolution TEM image in the STO [100] zone axis.

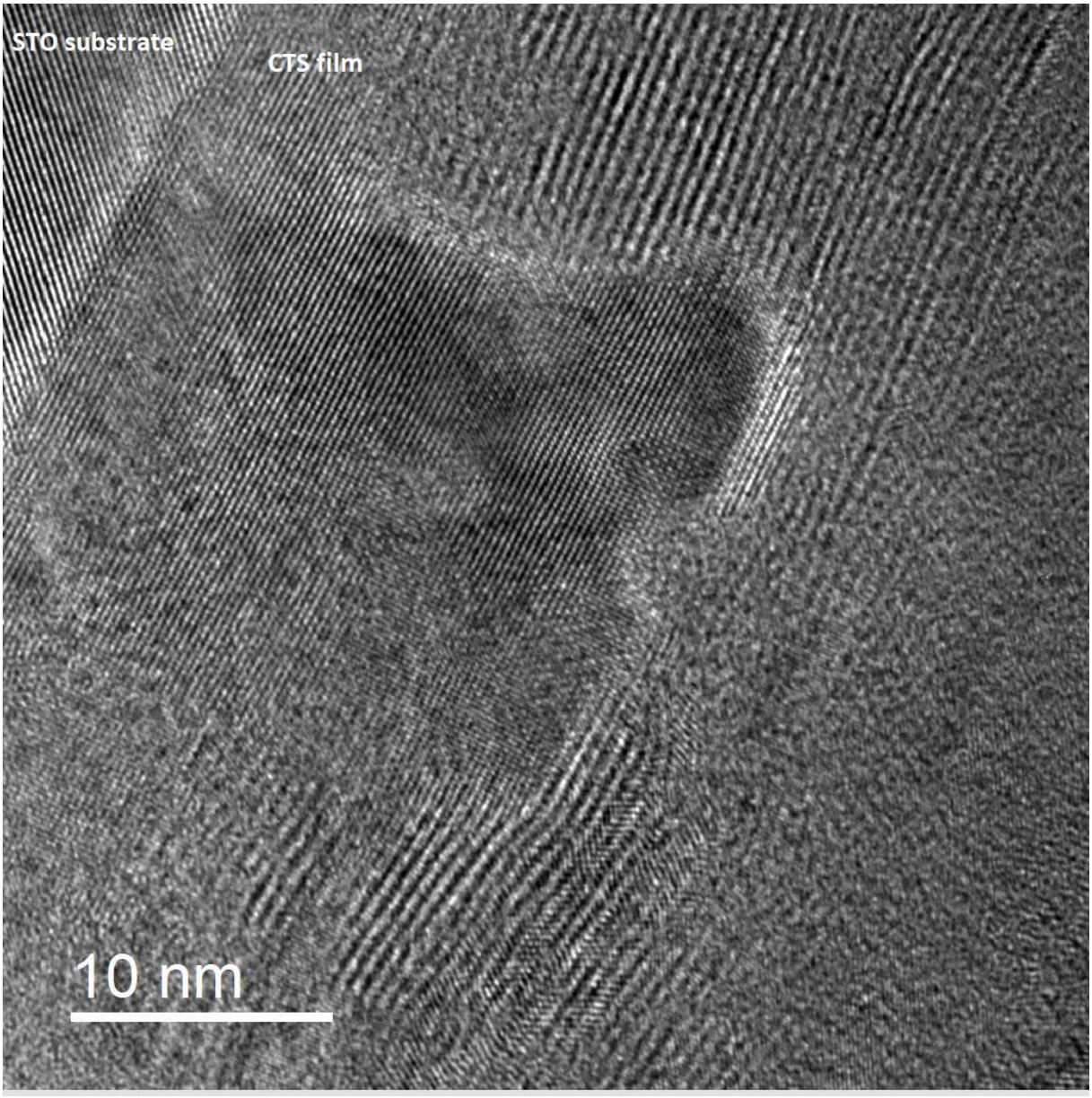

Table 1: Stoichiometry determined by EDS of the samples grown under different conditions such as substrate, deposition temperature and atmosphere.

Substrate	**Deposition temperature (°C)**	**Deposition atmosphere**	**Stoichiometry (EDS)**
STO (001)	600	vacuum	$\mathbf{Ca_1Ti_xS_{3.16}O_y}$
STO (001)	700	vacuum	$\mathbf{Ca_1Ti_xS_{3.11}O_y}$
STO (001)	800	vacuum	$\mathbf{Ca_1Ti_xS_{1.78}O_y}$
STO (001)	900	vacuum	$\mathbf{Ca_1Ti_xS_{0.71}O_y}$
STO (001)	600	10^{-3} mbar O_2	$\mathbf{Ca_1Ti_xO_y}$ **(S=0)**
STO (001)	600	10^{-2} mbar O_2	$\mathbf{Ca_1Ti_xO_y}$ **(S=0)**
ALO (0001)	600	vacuum	$\mathbf{Ca_1Ti_{1.05}S_{2.48}O_y}$
MAO (001)	600	vacuum	$\mathbf{Ca_1Ti_{0.92}S_{2.53}O_y}$

References:

[1] A. Swarnkar, W.J. Mir, R. Chakraborty, M. Jagadeeswararao, T. Sheikh, A. Nag, Are Chalcogenide Perovskites an Emerging Class of Semiconductors for Optoelectronic Properties and Solar Cell?, Chemistry of Materials, 31 (2019) 565-575. https://doi.org/10.1021/acs.chemmater.8b04178

[2] R.L.Z. Hoye, J. Hidalgo, R.A. Jagt, J.P. Correa-Baena, T. Fix, J.L. MacManus-Driscoll, The Role of Dimensionality on the Optoelectronic Properties of Oxide and Halide Perovskites, and their Halide Derivatives, Advanced Energy Materials, 12 (2022) 59. https://doi.org/10.1002/aenm.202100499

[3] S. Perera, H.L. Hui, C. Zhao, H.T. Xue, F. Sun, C.H. Deng, N. Gross, C. Milleville, X.H. Xu, D.F. Watson, B. Weinstein, Y.Y. Sun, S.B. Zhang, H. Zeng, Chalcogenide perovskites - an emerging class of ionic semiconductors, Nano Energy, 22 (2016) 129-135. https://doi.org/10.1016/j.nanoen.2016.02.020

[4] K.V. Sopiha, C. Comparotto, J.A. Marquez, J.J.S. Scragg, Chalcogenide Perovskites: Tantalizing Prospects, Challenging Materials, Advanced Optical Materials, 10 (2022) 27. https://doi.org/10.1002/adom.202101704

[5] S.Y. Niu, J. Milam-Guerrero, Y.C. Zhou, K. Ye, B.Y. Zhao, B.C. Melot, J. Ravichandran, Thermal stability study of transition metal perovskite sulfides, J. Mater. Res., 33 (2018) 4135-4143. https://doi.org/10.1557/jmr.2018.419

[6] Y.Y. Sun, M.L. Agiorgousis, P.H. Zhang, S.B. Zhang, Chalcogenide Perovskites for Photovoltaics, Nano Lett., 15 (2015) 581-585. https://doi.org/10.1021/nl504046x

[7] Z.B. Huo, S.H. Wei, W.J. Yin, High-throughput screening of chalcogenide single perovskites by first-principles calculations for photovoltaics, Journal of Physics D-Applied Physics, 51 (2018) 7. https://doi.org/10.1088/1361-6463/aae1ee

[8] S.A. Filippone, Y.Y. Sun, R. Jaramillo, The effect of an improved density functional on the thermodynamics and adsorption-controlled growth windows of chalcogenide perovskites, MRS Adv., 3 (2018) 3249-3254. https://doi.org/10.1557/adv.2018.497

[9] N.S. Rajput, H. Baik, J.Y. Lu, S.R. Tamalampudi, R. Sankar, A. Al Ghaferi, M. Chiesa, Revealing the Quasi-Periodic Crystallographic Structure of Self-Assembled SnTiS3 Misfit Compound, Journal of Physical Chemistry C, 125 (2021) 9956-9964. https://doi.org/10.1021/acs.jpcc.0c10756

[10] Y.E. Huang, W.L. Lin, C.G. Shi, L. Li, K.Q. Fan, X.Y. Huang, X.H. Wu, K.Z. Du, Misfit layer SnTiS3: An assemble-free van der Waals heterostructure SnS/TiS2 for lithium ion battery anode, Journal of Power Sources, 494 (2021) 8. https://doi.org/10.1016/j.jpowsour.2021.229712

[11] S.R. Tamalampudi, J.Y. Lu, N. Rajput, C.Y. Lai, B. Alfakes, R. Sankar, H. Apostoleris, S.P. Patole, I. Almansouri, M. Chiesa, Superposition of semiconductor and semi-metal properties of self-assembled 2D SnTiS3 heterostructures, npj 2D Mater. Appl., 4 (2020) 8. https://doi.org/10.1038/s41699-020-0158-7

[12] T. Fix, G. Schmerber, J.L. Rehspringer, M.V. Rastei, S. Roques, J. Bartringer, A. Slaoui, Insights on hexagonal TbMnO3 for optoelectronic applications: From powders to thin films, J. Alloy. Compd., 883 (2021) 6. https://doi.org/10.1016/j.jallcom.2021.160922

[13] H. Feng, S. Wang, B. Wu, The Phase Transition of Calcium Sulfide Under High Pressure, J. Phys.: Conf. Ser., 2148 (2022) 012015. https://doi.org/10.1088/1742-6596/2148/1/012015

[14] B. Liu, J. Yang, Y.H. Han, T.J. Hu, W.B. Ren, C.L. Liu, Y.Z. Ma, C.X. Gao, Electronic structure of TiS2 and its electric transport properties under high pressure, Journal of Applied Physics, 109 (2011) 5. https://doi.org/10.1063/1.3552299

[15] L.E. Conroy, K.C. Park, Electrical properties of the Group IV disulfides, titanium disulfide, zirconium disulfide, hafnium disulfide and tin disulfide, Inorg. Chem., 7 (1968) 459-463.

[16] A.H. Thompson, K.R. Pisharody, J. Koehler, R. F., Experimental Study of the Solid Solutions $Ti_xTa_{1-x}S_2$, Phys. Rev. Lett., 29 (1972) 163.

[17] F. Wooten, Optical Properties of Solids, Elsevier Inc., 1972.

[18] Y.L. Liao, W. Cao, J.W. Connell, Z.F. Chen, Y. Lin, Evolution of Moire Profiles from van der Waals Superstructures of Boron Nitride Nanosheets, Scientific Reports, 6 (2016) 10. https://doi.org/10.1038/srep26084
[19] M.A. Green, M.J. Keevers, Optical properties of intrinsic silicon at 300 K, Progr. Photovolt., 3 (1995) 189-192. https://doi.org/https://doi.org/10.1002/pip.4670030303